Optics Letters

Tailoring of spectral response and spatial field distribution with corrugated photonic crystal slab

Raanan Gad,[1,2,*] Wah Tung Lau,[3] Costa Nicholaou,[1,2] Soroosh Ahmadi,[1,2] Iliya Sigal,[1,2] and Ofer Levi[1,2]

[1]The Edward S. Rogers Sr. Department of Electrical and Computer Engineering, University of Toronto, 10 King's College Road, Toronto, Ontario M5S 3G4, Canada
[2]Institute of Biomaterials and Biomedical Engineering, University of Toronto, 164 College Street, Toronto, Ontario M5S 3G9, Canada
[3]Department of Physics, University of Toronto, 60 St. George Street, Toronto, Ontario M5S 1A7, Canada
*Corresponding author: raanan.gad@utoronto.ca

Received 1 May 2015; revised 15 July 2015; accepted 15 July 2015; posted 16 July 2015 (Doc. ID 240098); published 4 August 2015

We report a new physical mechanism for simultaneous tuning of quality factors, spectral responses, and field distributions in photonic crystal slabs through removal of polarization mode degeneracy using a lattice of elliptical nano-holes. The quality factors in these structures can become higher than those obtained with much smaller circular nano-holes. Furthermore, the modes can be superimposed by either rotating or morphing the elliptical nano-holes into a corrugated grating. These findings will enable improved radiation-matter interaction in optical, microwave, and THZ frequencies along with enhanced opto-acoustic coupling.

OCIS codes: (350.4238) Nanophotonics and photonic crystals; (260.3160) Interference; (220.0220) Optical design and fabrication; (050.2770) Gratings; (260.5430) Polarization.

http://dx.doi.org/10.1364/OL.40.003715

Controlling the interaction of light with periodic dielectric structures is critical for many optical devices, such as sensors [1], filters [2–4], quantum-optic devices [5], lasers [6], and light-assisted traps [7]. Moreover, dispersion engineering helps improve Microwave, RF, and THz systems [8,9], as well as dielectric laser accelerators [10] and optomechanic devices [11]. Periodic corrugated acoustic structures also enable flexible vibration control [12]. Last, dispersion tunability with strong coupling to electromagnetic fields and controllable anisotropy may enable reconfigurable metamaterials [13]. These resonators can benefit from fine tuning of their spectral response and spatial field distribution, while having relatively high-quality factors, Q. For example, spectral response shaping by interfering two resonances gives rise to electromagnetically induced transparency (EIT) like spectra [14].

Easy-to-fabricate photonic crystal slabs (PCSs) are an attractive platform to realize such large-area tunable resonators. Tuning the Fano resonance wavelengths and quality factors of PCSs is typically accomplished by arranging identical circular nano-holes (CNH) with radius r in a lattice with periodicity a, where r controls the quality factor, and a largely determines the resonance wavelength [15,16]. Fabrication technology limits the magnitudes of the achievable Qs in conventional PCSs, since high Qs require $r \ll a$ [17]. In addition, mode-polarization tuning is forbidden under the C_{4v} point group symmetry for normally incident radiation [18]. Various methods were explored to overcome the above limitations and control the PCS Fano resonance wavelength and Q [6,17,19].

Controlling sub-lattice fields' distributions is essential yet challenging for optimized light-matter interaction. Complex field distributions were obtained using different methods, e.g., coupling to high-order modes [19] and Band-Edge engineering [20, and references therein]. However, the former method typically shows low coupling efficiency, while the latter involves more than one wavefront interacting with the optical resonator to obtain the desired field patterns.

In this Letter, we demonstrate a new mechanism for spectral and spatial mode-shaping and quality-factor tuning of Fano resonances through mode-degeneracy removal, and show selective rearrangement and superposition of different fundamental (lowest order) modes. We realize this by patterning large aspect-ratio elliptical nano-holes (ENH), whose major axes are comparable to, or larger than, the lattice constants of the PCS. Such structural asymmetry lifts the polarization-mode degeneracy and creates a detuning of two distinct resonances of contrasting high and low Qs. In addition, we demonstrate lowering of fabrication tolerances required to obtain high Qs, thus removing the trade-off between Q and nano-hole size. Our findings can be readily scaled into other physical systems mentioned above.

PCS modes that couple to external continuum of radiation give rise to guided resonances (GR) [15]. With CNH, the fundamental GRs are two-fold degenerate under the C_{4v} point-group symmetry as shown in Fig. 1(a). Morphing the circle into an ellipse reduces the mode symmetry to C_{2v} as shown in Fig. 1(b). The supported GRs can be expressed as Bloch waves

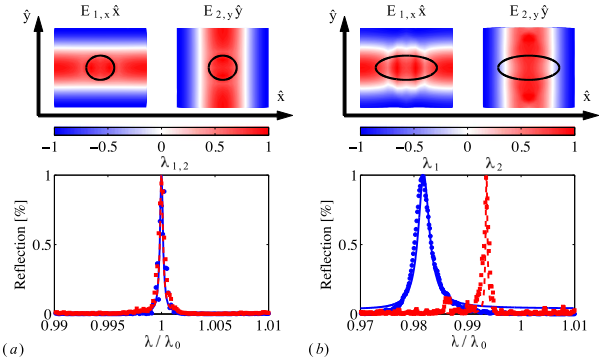

Fig. 1. Finite-difference time-domain (FDTD) simulations (solid and dashed lines), versus measured (circular and square markers), TE-like resonance for $\hat{x}$ (red) and $\hat{y}$ (blue) polarized, normally incident beam. Lattice periodicity: $a = 1050$ nm. The unit cell consisted of a nano-hole etched in a 160-nm-thick Si_3N_4 ($n = 2.02$) deposited on 5-μm-thick SiO_2 ($n = 1.46$). Index oil ($n = 1.402$) was applied on the patterned side of the PCS. (a) CNH with $r_x = r_y = 160$ nm, (b) ENH with $r_x = 460$ nm and $r_y = 160$ nm. Inset: FDTD simulation of E_x and E_y field patterns for $\hat{x}$ and $\hat{y}$ incident polarizations, respectively. All wavelengths are normalized to the resonance wavelength, $\lambda_0 = 1584$ nm of the circular nano-hole PCS.

$\boldsymbol{\Psi}_{\mathbf{k},m}(x, y, z)$ with band index m, and two dimensional (2D) wave-vector $\mathbf{k} = k_x\hat{x} + k_y\hat{y}$ in the form:

$$\boldsymbol{\Psi}_{\mathbf{k},m}(x, y, z) = e^{ik_x x + ik_y y}\mathbf{u}_{\mathbf{k},m}(x, y, z), \quad (1)$$

where $\mathbf{u}_{\mathbf{k},m}(x, y, z) = \mathbf{u}_{\mathbf{k},m}(x + N_x a, y + N_y a, z)$ for integers N_x and N_y with normalization $\delta_{m,m'} = \int_V \varepsilon(\mathbf{r})\mathbf{u}_{\mathbf{k},m}(\mathbf{r})\mathbf{u}^*_{\mathbf{k},m'}(\mathbf{r})\mathrm{d}^3\mathbf{r}$ over a unit cell volume V, where $\varepsilon(\mathbf{r})$ is the relative permittivity.

Assuming GRs are excited by plane waves at normal incidence ($k_{x,y} = 0$ and beam waist $\gg a$), the energy of the GRs decays primarily to the $k_{x,y} = 0$ plane-waves that propagate into the far field at both sides of the slab, provided that incident beam wavelength is below the first diffraction order, $\lambda > n \cdot a$, where n is the larger refractive index of both media outside the slab. Each of the incident plane-wave states has two-fold degeneracy with orthogonal-polarized components: $\boldsymbol{\xi}(\theta) = \hat{x}\cos\theta + \hat{y}\sin\theta$ and $\boldsymbol{\xi}(\theta + \pi/2) = -\hat{x}\sin\theta + \hat{y}\cos\theta$ for any polarization angle θ. ENH removes this degeneracy, allowing control of the polarization angles of the reflected beams.

Generally, for a square-lattice PCS with CNH, the fundamental modes at the Γ-point that can couple to the incident plane-wave states consist of a pair of orthogonal E_x- or E_y-dominated TE- and TM-like Bloch-modes. We focus our analysis on the TE-like modes, and similar analysis can be applied to TM-like modes. These modes feature an electric-field anti-node at the hole center as shown in the insets of Fig. 1(a). The in-plane electric field patterns are given by

$$\begin{aligned}\boldsymbol{\Phi}_1(x, y) &= A_1\{\hat{x}[(\sqrt{2}/a)\cos(2\pi y/a)] + \boldsymbol{\varphi}_1(x, y)\}\\ \boldsymbol{\Phi}_2(x, y) &= A_2\{\hat{y}[(\sqrt{2}/a)\cos(2\pi x/a)] + \boldsymbol{\varphi}_2(x, y)\}\end{aligned} \quad (2)$$

where $\boldsymbol{\varphi}_{1,2}(x, y)$ are small corrections due to in-plane dielectric modulations of the slab layer, adding small E_x- or E_y-field components to the leading terms, respectively. $A_{1,2}$ are normalization constants. For circular nano-hole PCS, the normalized field intensities in the hole and slab regions are equal for both orthogonal polarizations, resulting in a single resonance, as shown in Fig. 1(a). Such degeneracy is lifted with ENH, resulting in two spectrally distinct resonances with $\lambda_1 < \lambda_2$, as shown in Fig. 1(b). This spectral response is due to the alignment of the ellipse semi-major axis r_x with the anti-nodal plane of $\boldsymbol{\Phi}_1(x, y)$, while being perpendicular to $\boldsymbol{\Phi}_2(x, y)$, resulting in larger spatial overlapping of $|\boldsymbol{\Phi}_1(x, y)|^2$ with the low-index nano-hole region of $\varepsilon(x, y)$ as compared to $|\boldsymbol{\Phi}_2(x, y)|^2$.

Assuming that the contribution of the evanescent part of the mode outside the slab is either small or proportional to that inside the slab, the extent of coupling of the $\boldsymbol{\xi}(\theta)$-polarized plane-waves with these PCS modes is determined by their field-overlapping integral in a unit cell. This coupling is approximately proportional to the integral taken in mid-plane of the slab defined by:

$$\kappa_\alpha(\theta) \equiv \int_{-a/2}^{+a/2}\mathrm{d}x\int_{-a/2}^{+a/2}\mathrm{d}y\left[\varepsilon(x, y)\boldsymbol{\Phi}^*_\alpha(x, y)\cdot\frac{\boldsymbol{\xi}(\theta)}{a}\right], \quad (3)$$

where $\alpha = 1, 2$ denote the orthogonal pair of PCS modes, and the in-plane mode patterns are normalized as $\delta_{\alpha,\alpha'} = \int_{-a/2}^{+a/2}\mathrm{d}x\int_{-a/2}^{+a/2}\mathrm{d}y[\varepsilon(x, y)\boldsymbol{\Phi}^*_{\alpha'}(x, y)\cdot\boldsymbol{\Phi}_\alpha(x, y)]$. We can express $\kappa_\alpha(\theta) = \kappa_{\alpha,x}\cos\theta + \kappa_{\alpha,y}\sin\theta$, where $\kappa_{\alpha,x}$ and $\kappa_{\alpha,y}$ are the coupling constants of $\boldsymbol{\Phi}_\alpha(x, y)$ to the $\hat{x}$- or $\hat{y}$-polarized plane wave states. Using these quantities, we can define the coupling matrix, $\boldsymbol{\kappa}$, which relates the two incident polarization states to the two GRs by [15]:

$$\boldsymbol{\kappa} = \begin{bmatrix}\kappa_{1,x} & \kappa_{1,y}\\ \kappa_{2,x} & \kappa_{2,y}\end{bmatrix}. \quad (4)$$

The invariant $\gamma_\alpha \equiv (|\kappa_{\alpha,x}|^2 + |\kappa_{\alpha,y}|^2)/2$ is the total decay rate of the $\boldsymbol{\Phi}_\alpha(x, y)$ to both components of the $k_{x,y} = 0$ plane-wave states, and is also the linewidth of the resonance of $\boldsymbol{\Phi}_\alpha(x, y)$. With negligible material losses and negligible incoherent scattering, the quality factor Q_α of $\boldsymbol{\Phi}_\alpha(x, y)$ is solely dependent on the coupling to plane wave states, such that $Q_\alpha \sim 1/\gamma_\alpha$.

For ENHs aligned with the major and minor axes parallel to the x- and y-axes, $\varepsilon(x, y)$ is C_{2v} symmetric. Thus, off-diagonal elements in the coupling matrix in Eq. (4), $\kappa_{1,y}$ and $\kappa_{2,x}$, vanish. $\boldsymbol{\Phi}_1(x, y)$ and $\boldsymbol{\Phi}_2(x, y)$ couple only to the $\hat{x}$-, and $\hat{y}$-polarized plane-waves, respectively. As a result, when incident beam polarization is aligned with either the $\hat{x}$- (or $\hat{y}$-) axis, only a single resonance peak is excited at λ_1 (or λ_2), with the polarization preserved upon reflection or transmission, as shown in Fig. 1(b). As we tune the incident beam polarization angle θ from 0 to $\pi/2$, both resonances, $\lambda_{1,2}$, are excited and are blue-shifted with respect to λ_0 due to larger overall hole size. Thus, using ENH enables polarization-degeneracy removal and control over the coupling between external radiation and $\boldsymbol{\Phi}_\alpha(x, y)$.

We fabricated a set of square-lattice PCS samples, with the lattice parameters described in the caption of Fig. 1, to demonstrate PCS spectral response tuning using ENH. E-beam lithography was used to pattern the PCSs, while reactive ion etching was used to etch the nano-holes. The semi-minor radii were kept constant at $r_y = 160$ nm, while the semi-major radii

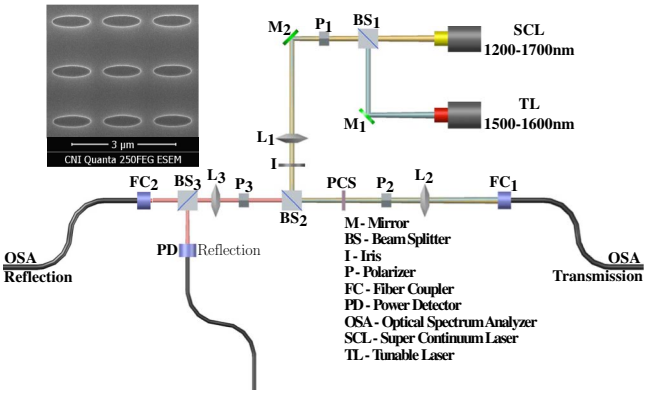

Fig. 2. Experimental setup used in the studies. Inset: SEM image of PCS with ENH patterned in 160-nm-thick Si_3N_4 on top of 5-μm-thick SiO_2.

r_x varied between 160 and 560 nm. The tilting angle of the ellipses' axes with respect to the lattice vectors was varied between $0 - \pi/2$. Uniform periodic patterns were obtained on samples as large as 0.1 mm^2 (inset of Fig. 2).

The experimental setup is presented in Fig. 2. The resonances were first located using a super-continuum source, followed by assessment of the resonance line-shapes using a tunable laser. Two polarizers along the optical path allow studying cross-polarization coupling between the orthogonal states.

The spectral responses of the fabricated PCSs were measured in the reflected pathway for two incident orthogonal polarizations, $\hat{x}$ and $\hat{y}$, and were compared to the simulated spectra, as shown in Fig. 1. The resonance wavelengths and line-widths of the $\mathbf{\Phi}_\alpha(x,y)$ modes were obtained by fitting Fano line-shapes to individual measured and simulated waveforms [15]. The

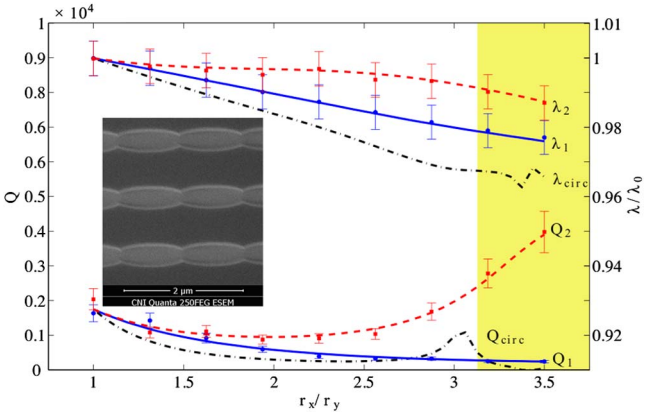

Fig. 3. Measured and simulated Q values (left axis) as a function of ENH aspect ratio: constant $r_y = 160$ nm, and varying $r_x = 160$–560 nm. Normalized resonance wavelength, $\lambda_0 = 1584$ nm, as a function of increased ENH aspect ratio (right axis). Measurements were performed for two incident beam polarizations: $\hat{x}$ (blue circular markers, Q_1 and λ_1) and $\hat{y}$ (red square markers, Q_2 and λ_2), with corresponding simulated results (blue solid lines and red dashed line). (dotted–dashed black line) Simulated result of CNH, with hole radius normalized to $r/160$ nm. Yellow-shaded region: transition region from 2D lattice to corrugated 1D grating. Inset: SEM image of a corrugated 1D grating.

results agree well with the theoretical predictions, which show the removal of mode-polarization degeneracy as the circular nano-hole is morphed into an elliptical one. Figure 3 shows a comparison between the measured and simulated (using freely available Fourier Modal Method software [21]) Qs of the $\mathbf{\Phi}_\alpha(x,y)$ modes as a function of the ENH aspect ratio for constant r_y, showing good agreement between the simulation and measurements (standard deviation of <15%).

Generally, the quality factor scales as $Q_\alpha \sim 1/(\lambda_\alpha \gamma_\alpha)$, and thus depends on the nano-holes' geometry. The shift in the resonance wavelength is relatively small as the ENH dimensions are changed, as demonstrated in Fig. 3. Thus, Q is dominated by the change in γ_α. According to Eq. (3) $\kappa_\alpha(\theta) = 0$, for an unpatterned slab, there is no coupling into the guided modes. Patterning the slab results in nonvanishing $\kappa_\alpha(\theta)$, giving rise to GRs. From Fig. 1(b), when the semi-major axis r_x of the ENH aligns with the anti-nodal plane of $\mathbf{\Phi}_1(x,y)$ to give a large $\kappa_{1,x}$, that also increases linearly with r_x, $Q_1 \sim (r_x/r_y)^{-2}$ monotonically decreases, as shown in Fig. 3. For $\hat{y}$-polarized incident beam, $\mathbf{\Phi}_2(x,y)$ is excited, the field contour that varies sinusoidally is parallel to the ENH major-axis, thus giving $Q_2 \sim |\sin(2\pi r_x/a)|^{-2}$ for $r_y \ll 0.5a$. Minimum Q is achieved when the hole region just overlaps with the node of $\mathbf{\Phi}_2(x,y)$. Increasing r_x beyond this node, $r_x > a/3$, reduces the overlap integral magnitude $|\kappa_{2,y}|$ and causes an increase in Q_2.

There is a continuous reduction in Q_1 as the structure morphs from a PCS to a 1D corrugated grating [see yellow shaded region in Fig. (3)]. Such transition explains the lower Qs of 1D gratings with respect to PCSs with the same layer structure. On the other hand, the resonance at λ_2 becomes very sharp with vanishingly small linewidth $\Delta\lambda_2 \sim |\kappa_{2,y}|^2/2$ as demonstrated in Fig. 3. Such high-Q resonance is of the same nature as the emergence of dark modes (modes that are decoupled from the radiation continuum) when a 1D grating is subjected to mild periodic modulation over its edges.

Similar modal analysis can help understand the trend in the resonance wavelengths, shown in Fig. 3. The resonance wavelength decreases in relative proportion to the increase in normalized field intensity $|\mathbf{\Phi}_\alpha(x,y)|^2$, as the low-index nano-hole region increases with r_x for both elliptical and CNH. The longest resonance wavelength is found for circular nano-hole PCSs due to the large nano-holes area.

These results suggest that relatively high-Q values can be obtained by fabricating structures with large nano-holes' area (comparable to a^2), and that these Qs can be tuned by changing the incident beam polarization. Furthermore, changing the input beam polarization enables selective excitation of nondegenerate resonances.

When the ENH axes are tilted with respect to lattice $\hat{x}$- and $\hat{y}$-vectors with angle $\eta > 0$, the PCS mode patterns, described by Eq. (2), deviate strongly from the leading terms as the field-correction terms $\boldsymbol{\varphi}_\alpha(x,y)$ increase in magnitude. In such a case, the off-diagonal elements of the coupling matrix, $\kappa_{1,y}$ and $\kappa_{2,x}$, become finite. The resonance peak separation $|\lambda_1 - \lambda_2|$ decreases for structures with elliptical semi-axes tilted toward $\pi/4$ from the $\hat{x}$- and $\hat{y}$-lattice vectors due to the spatial overlapping of $|\mathbf{\Phi}_\alpha(x,y)|^2$ with the tilted ENH region. Furthermore, when the tilting angle approaches $\pi/4$ and the aspect ratio is large,

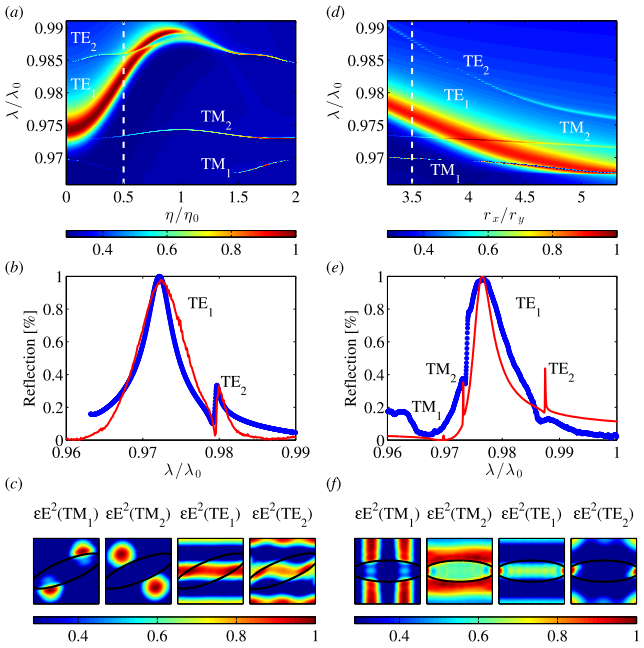

Fig. 4. PCS spectral and spatial mode tuning for tilted ENH and periodic-corrugated 1D grating, (a) simulated spectrum for tilted ENH with respect to lattice basis with $\eta = 0 - \pi/2$, $\eta_0 = \pi/4$, radii $r_y = 160$ nm, $r_x = 610$ nm, and incident beam polarization angle $\theta = 0$, (b) measured (blue dotted line) and simulated (red solid line) reflection spectrum for $\eta/\eta_0 = 0.5$ [dashed white line in (a), with the same dimensions and polarization as (a)], (c) the εE^2 patterns at the xy-cross-section, for TE- and TM-like modes of (b), (d) simulated spectrum versus aspect ratio for radii $r_y = 160$ nm, $r_x = 525$–850 nm, and incident beam polarization angle $\theta = \pi/8$, (e) measured (blue dotted line) and simulated (red solid line) reflection spectrum for $r_x/r_y = 3.5$ [dashed white line in (d)], (f) the εE^2 patterns at the xy cross-section, for TE- and TM-like modes of (e). The collected reflected light was measured with the same polarization of the incoming light beam.

λ_2 can be made close to λ_1, and the line-shape of λ_2 can be completely contained within that of λ_1, as shown in Fig. 4(a). Such spectral overlapping of both TE-like modes is experimentally demonstrated for a structure with tilting angle $\eta = \pi/8$, shown in Fig. 4(b). The corresponding mode patterns, in Fig. 4(c) show fine sub-wavelength features as $\mathbf{\Phi}_1(x, y)$ and $\mathbf{\Phi}_2(x, y)$ superimpose.

A complementary scheme to shape the spectral response and spatial field distribution is to use periodically corrugated 1D gratings, where the ENH semi-major axis $r_x > 0.5a$ such that neighboring nano-hole overlap. Here, the $TM_{1,2}$-like modes, with lower resonant wavelengths and higher Qs, can be made to superimpose over the low-Q TE_1-like modes. As shown in Fig. 4(d), the TE-like modes are blue-shifted as r_x increases, while the $TM_{1,2}$-like modes are significantly less sensitive to the change in r_x. The measurement of these resonances is shown Fig. 4(e), where the full, detailed line-shapes are well below the finest resolution we can measure. The resulting mode patterns from the superposition of TM- and TE-like modes are given in Fig. 4(f), where fine sub-wavelength features emerge similar to Fig. 4(c).

To summarize, we extend the capabilities of spectral and spatial-mode shaping in 2D photonic crystal lattices using elliptical nano-holes to remove polarization degeneracy. Transition from 2D to corrugated 1D structures can excessively overcome the conventional trade off in quality factor and nano-hole size in PCS structures. These findings will readily find applications in a variety of fields requiring dispersion engineering for improved radiation-matter interactions.

Funding. NSERC (RGPIN-03824-14; CHRP (CPG-121050); MITACS; CRANIA.

Acknowledgment. The authors are grateful for helpful discussions with Shanhui Fan and Victor Liu, Stanford University, Stanford, California.

REFERENCES

1. L. Marko, S. Axel, and Q. Yueming, Appl. Phys. Lett. **82**, 4648 (2003).
2. D. K. Jacob, S. C. Dunn, and M. Moharam, J. Opt. Soc. Am. A **18**, 2109 (2001).
3. T. Hitomichi, A. Yoshihiro, A. Takashi, and N. Susumu, Appl. Phys. Lett. **84**, 2226 (2004).
4. A.-L. Fehrembach, A. Talneau, O. Boyko, F. Lemarchand, and A. Sentenac, Opt. Lett. **32**, 2269 (2007).
5. P. Michler, A. Kiraz, C. Becher, W. Schoenfeld, P. Petroff, L. Zhang, E. Hu, and A. Imamoglu, Science **290**, 2282 (2000).
6. S. Noda, M. Yokoyama, M. Imada, A. Chutinan, and M. Mochizuki, Science **293**, 1123 (2001).
7. E. Jaquay, L. J. Martínez, C. A. Mejia, and M. L. Povinelli, Nano Lett. **13**, 2290 (2013).
8. A. Fernández-Domínguez, E. Moreno, L. Martin-Moreno, and F. Garcia-Vidal, Phys. Rev. B **79**, 233104 (2009).
9. J.-J. Wu, Prog. Electromagn. Res. **104**, 113 (2010).
10. R. J. England, R. J. Noble, K. Bane, D. H. Dowell, C.-K. Ng, J. E. Spencer, S. Tantawi, Z. Wu, R. L. Byer, E. Peralta, K. Soong, C.-M. Chang, B. Montazeri, S. J. Wolf, B. Cowan, J. Dawson, W. Gai, P. Hommelhoff, Y.-C. Huang, C. Jing, C. McGuinness, R. B. Palmer, B. Naranjo, J. Rosenzweig, G. Travish, A. Mizrahi, L. Schachter, C. Sears, G. R. Werner, and R. B. Yoder, Rev. Mod. Phys. **86**, 1337 (2014).
11. M. Aspelmeyer, T. J. Kippenberg, and F. Marquardt, Rev. Mod. Phys. **86**, 1391 (2014).
12. S. Banerjee and T. Kundu, J. Acoust. Soc. Am. **119**, 2006 (2006).
13. J.-Y. Ou, E. Plum, L. Jiang, and N. I. Zheludev, Nano Lett. **11**, 2142 (2011).
14. Y. Yang, I. I. Kravchenko, D. P. Briggs, and J. Valentine, Nat. Commun. **5**, 5753 (2014).
15. S. Fan and J. Joannopoulos, Phys. Rev. B **65**, 235112 (2002).
16. S. Peng and G. M. Morris, Opt. Lett. **21**, 549 (1996).
17. J. Lee, B. Zhen, S.-L. Chua, W. Qiu, J. D. Joannopoulos, M. Soljačić, and O. Shapira, Phys. Rev. Lett. **109**, 067401 (2012).
18. K. Sakoda, *Optical Properties of Photonic Crystals* (Springer, 2005).
19. O. Kilic, M. Digonnet, G. Kino, and O. Solgaard, Opt. Express **16**, 13090 (2008).
20. E. Miyai, K. Sakai, T. Okano, W. Kunishi, D. Ohnishi, and S. Noda, Nature **441**, 946 (2006).
21. V. Liu and S. Fan, Comput. Phys. Commun. **183**, 2233 (2012).